Spin scattering and noncollinear spin structure-induced intrinsic anomalous Hall effect in antiferromagnetic topological insulator MnBi$_2$Te$_4$

Seng Huat Lee [1,2,*] Yanglin Zhu,[2,3,*] Yu Wang,[1,2] Leixin Miao,[4] Timothy Pillsbury,[2] Hemian Yi,[2] Susan Kempinger,[2]
Jin Hu,[5] Colin A. Heikes,[6] P. Quarterman,[6] William Ratcliff,[6] Julie A. Borchers,[6] Heda Zhang,[7] Xianglin Ke,[7] David Graf,[8]
Nasim Alem,[4] Cui-Zu Chang,[1,2] Nitin Samarth,[1,2] and Zhiqiang Mao[1,2,†]

[1]*2D Crystal Consortium, Materials Research Institute, Pennsylvania State University, University Park, Pennsylvania 16802, USA*
[2]*Department of Physics, Pennsylvania State University, University Park, Pennsylvania 16802, USA*
[3]*Department of Physics and Engineering Physics, Tulane University, New Orleans, Louisiana 70118, USA*
[4]*Department of Materials Science and Engineering, Pennsylvania State University, University Park, Pennsylvania 16802, USA*
[5]*Department of Physics, University of Arkansas, Fayetteville, Arkansas 72701, USA*
[6]*NIST Center for Neutron Research, National Institute of Standards and Technology, Gaithersburg, Maryland 20899, USA*
[7]*Department of Physics and Astronomy, Michigan State University, East Lansing, Michigan 48824, USA*
[8]*National High Magnetic Field Laboratory, Tallahassee, Florida 32310, USA*

MnBi$_2$Te$_4$ has recently been established as an intrinsic antiferromagnetic (AFM) topological insulator—an ideal platform to create quantum anomalous Hall insulator and axion insulator states. We performed comprehensive studies on the structure, nontrivial surface state, and magnetotransport properties of this material. Our results reveal an intrinsic anomalous Hall effect arising from a noncollinear spin structure for the magnetic field parallel to the c axis. We observed negative magnetoresistance under arbitrary field orientation below and above the Néel temperature (T_N), providing clear evidence for strong spin fluctuation-driven spin scattering in both the AFM and paramagnetic states. Furthermore, we found that the nontrivial surface state opens a large gap ($\sim$85 meV) even far above T_N. Our findings demonstrate that the bulk band structure of MnBi$_2$Te$_4$ is strongly coupled with the magnetic property and that a net Berry curvature in momentum space can be created in the canted AFM state. In addition, our results imply that the gap opening in the surface states is intrinsic, likely caused by the strong spin fluctuations in this material.

The recently discovered quantum anomalous Hall (QAH) effect [1–7] is a variant of the Chern insulator first envisioned by Haldane [8]. Characterized by a quantized Hall conductance and vanishing longitudinal conductance at zero magnetic field, the QAH requires combining topology with magnetism [2,6,7]. This can be achieved in three ways: magnetic doping of a topological insulator (TI) [3,4], proximity of a TI to a ferromagnetic (FM) or an antiferromagnetic (AFM) insulator [9–15], or in TIs that are intrinsically FM or AFM [16]. The true QAH effect has only been seen in thin TI films of Cr- and/or V-doped (Bi, Sb)$_2$Te$_3$ [3,4]. However, the "critical temperature" required is below $\sim$2 K [3,4,17,18], severely constraining the exploration of fundamental physics and technological applications. The recent discovery of an intrinsic AFM TI, MnBi$_2$Te$_4$ [19–21], predicted to show a high-temperature QAH effect in thin films is a key advance in this context.

MnBi$_2$Te$_4$ crystallizes in a rhombohedral structure with the space group $R\bar{3}m$ [22], built of the stacking of Te-Bi-Te-Mn-Te-Bi-Te septuple layers (SLs) along the c axis [inset of Fig. 1(b)]. The antiferromagnetism of this material is produced by the Mn sublattice, while its nontrivial surface state is formed by inverted Bi and Te p_z bands at the Γ point due to strong spin-orbit coupling (SOC). Since its AFM state is characterized by an A-type AFM order ($T_N = 25$ K) [21], formed by the Mn FM layers stacked antiferromagnetically along the c axis [21,23], the FM layer near the cleavage surface is anticipated to break time-reversal symmetry (TRS), thus opening a large gap ($\sim$50 or 88 meV [20,21,24]) in the topological surface state; this has been probed in angle-resolved photoemission spectroscopy (ARPES) measurements on single-crystal samples [21,24].

MnBi$_2$Te$_4$ is expected to be an ideal quantum material for hosting interesting topological phases, including a high-temperature QAH insulator in thin films with odd numbers of SLs [19,20,25], an axion insulator state [9,19] exhibiting the topological magnetoelectric effect in thin films with even numbers of SLs, an ideal Weyl semimetal state with a single pair of Weyl nodes near the Fermi level [19,20], and possibly chiral Majorana modes via interaction with an s-wave superconductor [26]. Recently, both the magnetic-field-driven quantized Hall state (Chern insulator) and the axion insulator at zero field have been observed in exfoliated MnBi$_2$Te$_4$

*These authors contributed equally to this work.
†zim1@psu.edu
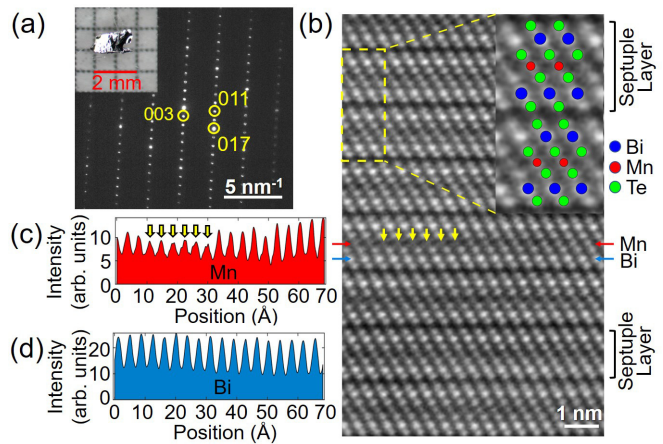
FIG. 1. (a) The selected area diffraction pattern taken from the [100] zone axis for MnBi$_2$Te$_4$. Inset: Crystal image of MnBi$_2$Te$_4$. (b) HAADF-STEM image taken from the [100] zone axis. Inset: Magnified image of a one-unit cell with the atoms overlaid on top to demonstrate the layered structure of MnBi$_2$Te$_4$. The yellow arrows in (b) mark Mn vacancies. (c) and (d) The intensity profiles of Mn and Bi atomic columns indicated by the red and blue arrows in (b).

thin films [27,28], which makes this material a fascinating playground for the study of topological quantum states.

In this Rapid Communication, we report a systematic study of single-crystal samples of MnBi$_2$Te$_4$, focusing on elucidating the coupling between bulk electronic and magnetic properties, as well as exploring how surface states are related to magnetism. Our studies reveal clear evidence of spin fluctuation-driven spin scattering in both the AFM ordered state and the paramagnetic (PM) state above T_N, suggesting that the opening of a gap in the nontrivial surface states in the PM state is likely driven by the strong spin fluctuations in this material. Moreover, we observed an intrinsic anomalous Hall effect not linearly coupled with magnetization in a canted AFM phase for the fields applied along the c axis, indicating the presence of a net Berry curvature in momentum space created by the noncollinear spin structure. These findings would advance understanding of the underlying physics of this exciting material.

MnBi$_2$Te$_4$ single crystals [inset of Fig. 1(a)] were synthesized using the melt growth method [21] [see the Supplemental Material (SM) [29] for details]. The structure of MnBi$_2$Te$_4$ crystals were analyzed using x-ray diffraction (Fig. S1) and high-resolution scanning transmission electron microscope (STEM) imaging. The dotlike diffraction spots seen in the electron diffraction pattern taken along the [100] zone axis [Fig. 1(a)] indicate the single crystallinity of the sample with no stacking faults between SLs. The atomic resolution high angle annular dark field (HAADF)-STEM image taken along the [100] zone axis clearly demonstrates the layered structure of MnBi$_2$Te$_4$ comprising the stacking of Te-Bi-Te-Mn-Te-Bi-Te SLs along the c axis [Fig. 1(b)] [22]. Figures 1(c) and 1(d) show the uniform intensity line profile of Mn and Bi atoms, delineated by red and blue arrows in the STEM image, indicating little to no intermixing of the two elements. Additionally, within the Mn intensity line profile, peaks with lower Mn intensity can be seen (marked by yellow arrows), indicating
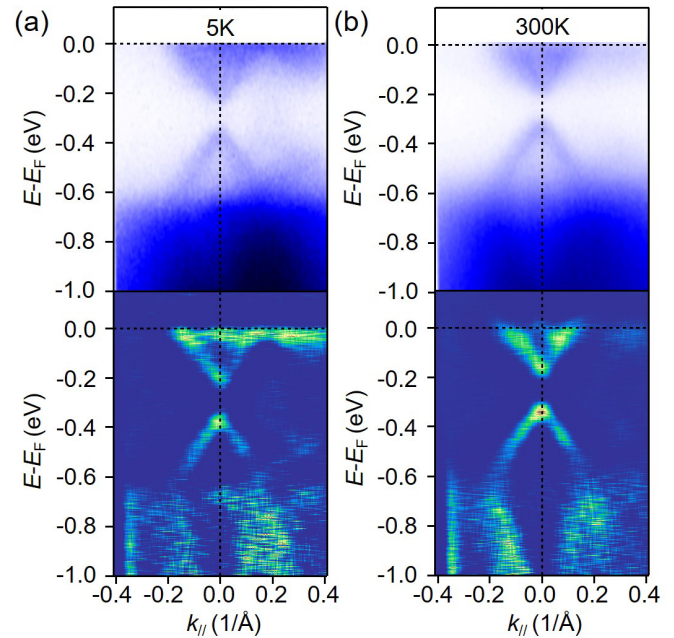

FIG. 2. ARPES band maps of MnBi$_2$Te$_4$ single crystal along the $K-\Gamma-K$ direction and the corresponding second derivative maps at (a) 5 K and (b) 300 K.

Mn vacancies within the atomic column. Mn vacancies can also be distinguished in the bright field (BF) and low angle annular dark field (LAADF)-STEM images (Fig. S2) and the resulting strain contrast associated with them.

A key signature of the AFM TI state in MnBi$_2$Te$_4$ is that its surface with preserved S symmetry has a gapless Dirac cone, while the surface with broken S symmetry is characterized by a Dirac cone with a large gap (50 or 88 meV [20,21]). S stands for a combined symmetry, defined as $S = \Theta T_{1/2}$, where Θ represents TRS and $T_{1/2}$ denotes primitive-lattice transition symmetry [30]. The (001) surface, the cleavage plane, is an S-symmetry broken surface in the AFM state and should thus have a gapped Dirac cone [20]. Such a gapped Dirac cone has recently been probed in the ARPES band maps of single-crystal samples [21,24]; the gap magnitude measured at the Γ point is $\sim$70 meV at 17 K, consistent with the theoretically calculated gap [19,20]. We also performed ARPES measurements on our MnBi$_2$Te$_4$ single-crystal samples and observed clear signatures of gapped surface states at both 5 and 300 K, as shown in Figs. 2(a) and 2(b). The gap magnitude is $\sim$85 meV at both temperatures, consistent with the previous ARPES studies [21,24]. This observation indicates that the gap opening observed here does not originate from the AFM order in MnBi$_2$Te$_4$. We speculate such a surface state gap opening in MnBi$_2$Te$_4$ is driven by spin fluctuations in the PM phase, as discussed below.

Using magnetic susceptibility measurements on MnBi$_2$Te$_4$ [Fig. S3(a)], we observed an AFM transition at $\sim$25 K with the spin-easy axis along the c axis. The isothermal magnetization measurements for $H \parallel c$ [Figs. 3(a) and S3(b)] reveal a remarkable spin-flop transition near 3.57 T at 2 K (denoted by H_{c1} hereafter), which leads the system to a metastable canted AFM (CAFM) state. The noncollinear spin structure of the CAFM phase is verified by neutron scattering measurements,
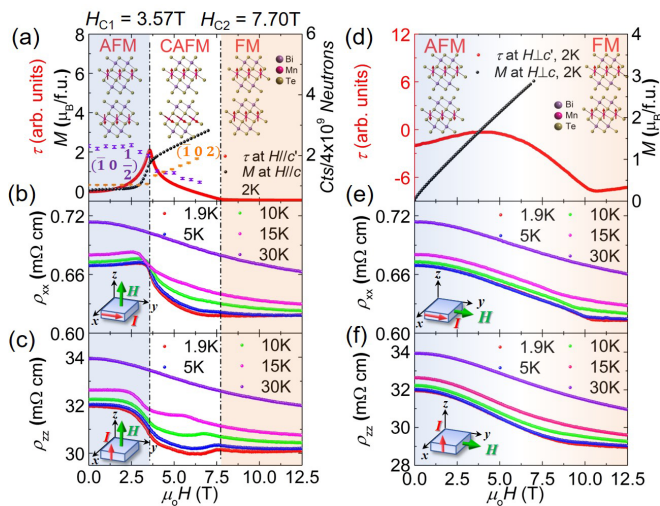
FIG. 3. (a) and (d): Field dependence of magnetic torque τ of $MnBi_2Te_4$ at 2 K for (a) $H \parallel c'$ and (d) $H \perp c'$ (c' denotes a direction nearly parallel to the c axis). The purple and orange data points in (a) are the neutron scattering intensities at $(\bar{1}0\frac{1}{2})$ and $(\bar{1}02)$ as a function of magnetic field at 4.2 K. Error bars represent one sigma errors based on Poisson counting statistics. The black curves in (a) and (d) represent the isothermal magnetization measured at 2 K with $H \parallel c$ and $H \perp c$. The insets illustrate the antiferromagnetic (AFM), canted antiferromagnetic (CAFM), and ferromagnetic (FM) phases in the different field ranges. (b) and (c): Field dependences of in-plane resistivity ρ_{xx} and out-of-plane resistivity ρ_{zz} at various temperatures for $H \parallel c$. (e) and (f): Field dependences of ρ_{xx} and ρ_{zz} at various temperatures for $H \perp c$. The insets in (b), (c), (e), and (f) illustrate the experiment setups.

which finds the AFM reflection peak $(\bar{1}0\frac{1}{2})$ intensity decreases at magnetic fields above 3 T, while the FM diffraction peak $(\bar{1}02)$ intensity increases, with an inflection point near 3.5 T (see Sec. 5 in SM for details). Moreover, we also conducted magnetic torque measurements and found the transition from the CAFM to FM phase occurs at ~7.70 T (denoted by H_{c2}), as shown in Fig. 3(a). The measured torque is not directly proportional to magnetization, but dependent on the components of the magnetization and magnetic field along the c axis and in-plane directions of the sample, as explained in the SM (Sec. 6). In Fig. 3(a), we also include schematics of three distinct magnetic phases (i.e., AFM, CAFM, and FM) in the different field ranges. However, the metamagnetic transition does not appear for $H \perp c$. The isothermal magnetization measured at 2 K for $H \perp c$ displays a linear field dependence [Fig. 3(d)], indicating that the AFM state is gradually polarized to a FM state. The high-field torque [Fig. 3(d)] and magnetotransport measurements [Figs. 3(e) and 3(f)] indicate the full FM polarization occurs around 10.5 T.

Figures 4(a) and 4(b) present the temperature dependences of the in-plane (ρ_{xx}) and out-of-plane (ρ_{zz}) resistivity under different magnetic fields ($H \parallel c$). Both $\rho_{xx}(T)$ and $\rho_{zz}(T)$ at zero field exhibit metallic behavior above 40 K with a moderate electronic anisotropy ($\rho_{zz}/\rho_{xx} \sim 35$ at 2 K) and remarkable peaks at the AFM transition. Such resistivity peaks near T_N can be well understood in terms of spin scattering due to spin fluctuations as discussed below. In general, in AFM
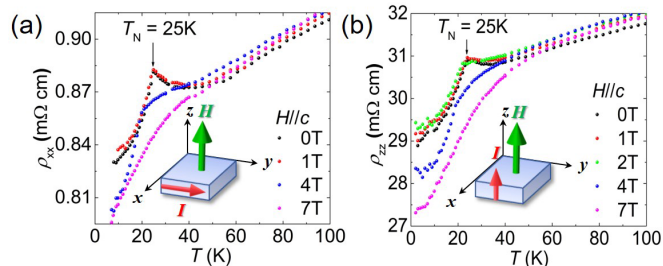

FIG. 4. Temperature dependences of the (a) in-plane resistivity ρ_{xx} and (b) out-of-plane resistivity ρ_{zz} under various magnetic fields ($H \parallel c$).

or FM materials, spin fluctuations always tend to intensify as the temperature approaches the ordering temperature where they reach maximum strength. For a local-moment AFM state, the intensified spin fluctuations due to spin-wave excitations near T_N can greatly affect transport properties through spin scattering if itinerant carriers interact with local moments. This results in a resistivity peak near T_N. Such a scenario was previously demonstrated in an AFM material $Fe_{1+y}Te$ [31]. The resistivity peak near T_N observed here should follow a similar mechanism.

We systematically measured the variation of resistivity under an external magnetic field. Figures 4(a) and 4(b) show that the peaks near T_N in both $\rho_{xx}(T)$ and $\rho_{zz}(T)$ are suppressed by the magnetic fields higher than H_{c1}. This observation is consistent with the spin fluctuation-driven spin-scattering scenario. Further, for an A-type AFM system, interlayer AFM coupling usually generates strong spin scattering in the ordered state, resulting in a high-resistivity state. However, when the applied field is strong enough to overcome the interlayer AFM coupling and push it to a forced FM state, the spin scattering would be suppressed, resulting in a low-resistivity state. Such a phenomenon is termed as a spin-valve effect and was first demonstrated in magnetic, multilayer thin films [32,33]. The spin-valve effect can also occur between an A-type AFM and a CAFM state as seen in $Ca_3Ru_2O_7$ [34]. We indeed observed a similar spin-valve effect in the magnetotransport measurements of $MnBi_2Te_4$, as shown below.

We performed magnetic field sweep measurements of both ρ_{xx} and ρ_{zz} at various temperatures for both $H \parallel c$ and $H \perp c$, as presented in Fig. 3. For $H \parallel c$, $\rho_{xx}(H)$ and $\rho_{zz}(H)$ show a steep decrease in response to the AFM-to-CAFM transition at H_{c1} [Figs. 3(b) and 3(c)], consistent with the expected spin-valve behavior, indicating the interlayer AFM ordering results in strong spin scattering. When the system is across the CAFM-to-FM transition at H_{c2}, $\rho_{xx}(H)$ is constant, while $\rho_{zz}(H)$ displays a little hump at H_{c2} which shifts to lower field at higher temperatures. These observations suggest that the spin scattering due to the interlayer AFM coupling is mostly suppressed in the CAFM phase. The little hump near H_{c2} observed in $\rho_{zz}(H)$ is likely due to the fact that the magnetoresistivity also contains a positive term induced by the Lorentz effect and anisotropic Fermi surface, as evidenced by the data measured above 15 T (Fig. S7).

The suppression of spin scattering by magnetic field is also observed in $\rho_{xx}(H)$ and $\rho_{zz}(H)$ measurements for $H \perp c$
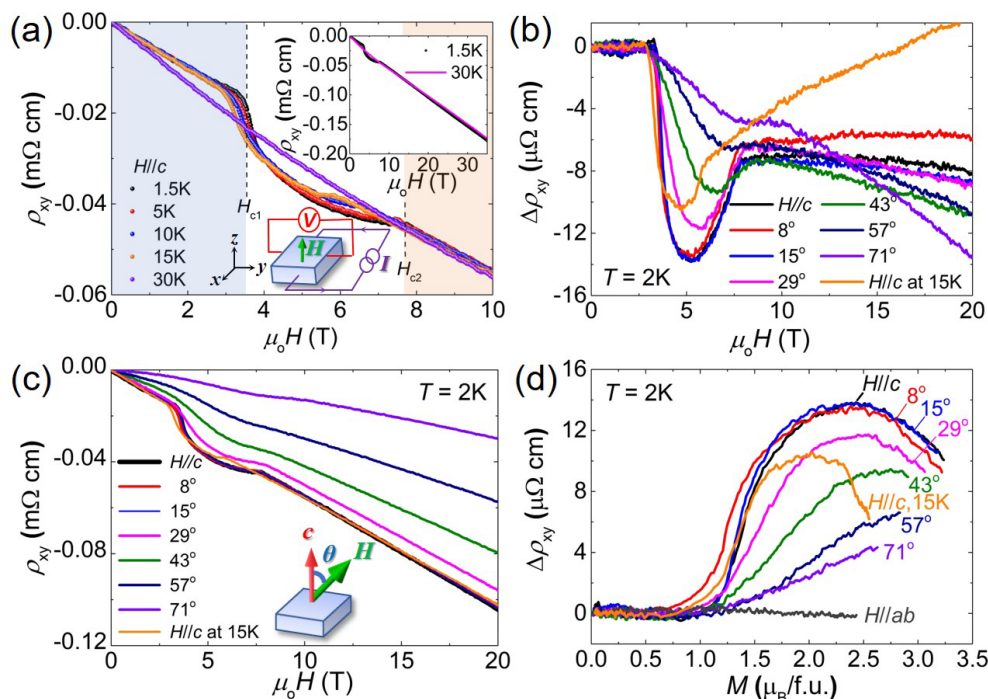
FIG. 5. (a) Hall resistivity ρ_{xy} as a function of magnetic field at various temperatures for MnBi$_2$Te$_4$. The schematic illustrates the experimental setup for ρ_{xy} measurements. Inset: ρ_{xy} vs H in the 0–35 T field range at 1.5 and 30 K. (b) The field dependence of anomalous Hall resistivity $\Delta\rho_{xy}$ under various field orientations, obtained after subtracting the normal Hall resistivity due to the Lorentz effect from ρ_{xy} shown in (c). (c) Hall resistivity as a function of magnetic field under various field orientations. (d) $\Delta\rho_{xy}$ plotted against the magnetization M for different field orientations. The data in orange color were collected at 15 K and the rest were measured at 2 K [the magnetization data used for making this plot are shown in Fig. S3(c)].

[Figs. 3(e) and 3(f)]. Since the AFM phase is gradually polarized to a FM state in this field configuration [Fig. 3(d)], $\rho_{xx}(H)$ and $\rho_{zz}(H)$ show a gradual decrease with increasing field and then tend to level off near H_{c2}. In addition to observing spin scattering in the AFM state, we also found spin scattering is substantial in the PM state, as evidenced by the large negative magnetoresistance (MR) at $T = 30$ K for both $H \parallel c$ and $H \perp c$ [e.g., $[\rho_{zz}(H) - \rho_{zz}(0)]/\rho_{zz}(0) \sim -6\%$ to -9% at 12.5 T and 30 K, comparable to the magnitude of negative MR seen in the AFM state in the same field range]. These results strongly support that the PM state has strong spin fluctuations. Since the intralayer Mn-Te-Mn FM superexchange interactions are much stronger than the interlayer AFM interaction, the spin fluctuations in the PM state should feature FM correlation (i.e., FM spin fluctuations), as manifested in the positive Curie-Weiss temperature ($\theta_{CW} \sim$ 5 K) extracted from the susceptibility [inset of Fig. S3(a)]. Such strong FM fluctuations might break TRS symmetry, thus resulting in the gap opening of surface states as observed in ARPES experiments (Fig. 2). The spin fluctuation-driven gap opening in the nontrivial surface state in magnetic doped TIs has indeed been established in previous work [35]. We note the gap magnitude of the surface states hardly varies with temperature (Fig. 2), which is consistent with previous reports [21,24] and can possibly be attributed to the strong spin fluctuations arising from intralayer Mn-Te-Mn FM superexchange interactions.

Another possible consequence of strong spin scattering is low transport mobility. This is also verified in our Hall

resistivity ρ_{xy} measurements. Figure 5(a) shows ρ_{xy} as a function of magnetic field at various temperatures. From these data, we found the carrier mobility is indeed low. However, we observed an intrinsic anomalous Hall (AH) effect in the CAFM phase. When the field is increased above H_{c2}, all the data taken at different temperatures collapse onto a single line up to the maximum measurement field 35 T [inset of Fig. 5(a)], consistent with the single-band nature of this system. The Hall coefficient R_o extracted from such a linear field dependence of ρ_{xy} is -4.76×10^{-10} Ω cm/Oe, from which the carrier mobility μ ($= R_o/\rho_{xx}$) is estimated to 79 cm^2/V s at 30 K, much less than the carrier mobility in bulk Bi$_2$Te$_3$ ($>$800 cm^2/V s) [36,37]. The carrier density estimated from R_o is 1.31×10^{20} cm^{-3}, falling into the carrier density range of Bi$_2$Te$_3$ ($10^{17}-10^{20}$ cm^{-3}) [37,38]. The negative sign of R_o indicates that the carriers in our samples are electron type, consistent with the ARPES measurement results (Fig. 2).

Next, we focus on the intrinsic AH effect observed in the CAFM phase. The ρ_{xy} of this phase shows striking humplike features for $H \parallel c$, contrasted with the linear field dependence in the AFM phase below H_{c1} and the FM phase above H_{c2} [Fig. 5(a)]. The anomalous hump is gradually suppressed as the field is tilted toward the in-plane direction [Fig. 5(c)]. Since the linear increase of ρ_{xy} above H_{c2} is due to the normal Hall resistivity ρ_{xy}^N, we obtain the AH resistivity $\Delta\rho_{xy}$ after subtracting ρ_{xy}^N, as shown in Fig. 5(b), where $\Delta\rho_{xy}$ under various field orientations is also presented. $\Delta\rho_{xy}$ can be further expressed as $\Delta\rho_{xy} = \rho_{xy}^A + \rho_{xy}^T$ [39], where ρ_{xy}^A represents the AH resistivity linearly coupled to the magnetization, whereas

ρ_{xy}^T stands for the AH resistivity due to the net Berry curvature in the momentum space caused by the noncollinear spin structure. ρ_{xy}^A arises from the combination of the extrinsic (the skew scattering and the side jump) and intrinsic contributions and is proportional to magnetization [40]. To separate ρ_{xy}^T from $\Delta\rho_{xy}$, we plot $\Delta\rho_{xy}$ as a function of magnetization M in Fig. 5(d) [note the magnetization data under various field orientations are shown in Fig. S3(c)]. We find $\Delta\rho_{xy}(M)$ is nearly linear for the AFM phase below H_{c1}, but exhibits significant humps due to the presence of ρ_{xy}^T in the CAFM phase [Fig. 5(d)]. The maximum ρ_{xy}^T for $H \parallel c$ reaches $\sim 14\,\mu\Omega$ cm, more than twice that seen in the chiral antiferromagnet Mn_3Sn [41]. The angular dependence of $\Delta\rho_{xy}(M)$ in Fig. 5(d) shows ρ_{xy}^T is strongly suppressed for $\theta > 50°$. Additionally, we also analyzed $\Delta\rho_{xy}(M)$ of $H \parallel c$ at 15 K where H_{c1} and H_{c2} can be directly probed from magnetization [Fig. S3(c)] and find the ρ_{xy}^T component of the CAFM phase is also significant at this temperature [Fig. 5(d)].

A large ρ_{xy}^T is generally expected for an AFM state with noncollinear spin structure [42]. Symmetry breaking plus strong SOC in such systems can lift spin degeneracy, which can lead to a net Berry curvature in momentum space, thus resulting in an intrinsic AH effect. As indicated above, the noncollinear spin structure of the CAFM phase is evidenced by both the magnetization and neutron scattering measurements. Therefore, the large ρ_{xy}^T value of the CAFM phase can be reasonably attributed to the noncollinear spin structure. This result implies the electronic band structure of $MnBi_2Te_4$ is strongly coupled to its magnetism, offering an opportunity to observe different topological states tuned by a magnetic field. Theoretical studies have shown the AFM TI state can evolve into an ideal Weyl semimetal state when the system transforms into a FM phase under magnetic field. However, we did not observe any transport signatures of a Weyl state in the FM phase (such as chiral anomaly) probably because of the Weyl node far from the Fermi level.

In summary, the strong coupling between electronic and magnetic properties of $MnBi_2Te_4$ provides clear evidence of spin scattering in both the AFM and PM states. We attribute the strong spin scattering in the PM state to spin fluctuations that open a gap in the surface states above T_N. Moreover, we find a canted AFM state that exhibits an intrinsic AH effect as a result of the net Berry curvature in the momentum space induced by the noncollinear spin structure, indicating that the electronic band structure of $MnBi_2Te_4$ is strongly coupled with magnetism. Given this material has been demonstrated to host axion insulator and Chern insulator phases, our findings will be important for further understanding of this fascinating material.

[1] C.-X. Liu, X.-L. Qi, X. Dai, Z. Fang, and S.-C. Zhang, Phys. Rev. Lett. **101**, 146802 (2008).

[2] R. Yu, W. Zhang, H. J. Zhang, S. C. Zhang, X. Dai, and Z. Fang, Science **329**, 61 (2010).

[3] C. Z. Chang *et al.*, Science **340**, 167 (2013).

[4] C. Z. Chang, W. Zhao, D. Y. Kim, H. Zhang, B. A. Assaf, D. Heiman, S.-C. Zhang, C. Liu, M. H. W. Chan, and J. S. Moodera, Nat. Mater. **14**, 473 (2015).

[5] C.-X. Liu, S.-C. Zhang, and X.-L. Qi, Annu. Rev. Condens. Matter Phys. **7**, 301 (2016).

[6] C.-Z. Chang and M. Li, J. Phys.: Condens.: Matter **28**, 123002 (2016).

[7] K. He, Y. Wang, and Q.-K. Xue, Annu. Rev. Condens. Matter Phys. **9**, 329 (2018).

[8] F. D. M. Haldane, Phys. Rev. Lett. **61**, 2015 (1988).

[9] X.-L. Qi, T. L. Hughes, and S.-C. Zhang, Phys. Rev. B **78**, 195424 (2008).

[10] P. Wei, F. Katmis, B. A. Assaf, H. Steinberg, P. Jarillo-Herrero, D. Heiman, and J. S. Moodera, Phys. Rev. Lett. **110**, 186807 (2013).

[11] Z. Jiang, C.-Z. Chang, C. Tang, P. Wei, J. S. Moodera, and J. Shi, Nano Lett. **15**, 5835 (2015).

[12] F. Katmis *et al.*, Nature (London) **533**, 513 (2016).

[13] Z. Jiang, C.-Z. Chang, M. R. Masir, C. Tang, Y. Xu, J. S. Moodera, A. H. MacDonald, and J. Shi, Nat. Commun. **7**, 11458 (2016).

[14] H. Wang, J. Kally, J. S. Lee, T. Liu, H. Chang, D. R. Hickey, K. A. Mkhoyan, M. Wu, A. Richardella, and N. Samarth, Phys. Rev. Lett. **117**, 076601 (2016).

[15] C. Tang *et al.*, Sci. Adv. **3**, e1700307 (2017).

[16] P. Tang, Q. Zhou, G. Xu, and S.-C. Zhang, Nat. Phys. **12**, 1100 (2016).

[17] M. Mogi, R. Yoshimi, A. Tsukazaki, K. Yasuda, Y. Kozuka, K. S. Takahashi, M. Kawasaki, and Y. Tokura, Appl. Phys. Lett. **107**, 182401 (2015).

[18] Y. B. Ou *et al.*, Adv. Mater. **30**, 1703062 (2018).

[19] D. Zhang, M. Shi, T. Zhu, D. Xing, H. Zhang, and J. Wang, Phys. Rev. Lett. **122**, 206401 (2019).

[20] J. Li, Y. Li, S. Du, Z. Wang, B.-L. Gu, S.-C. Zhang, K. He, W. Duan, and Y. Xu, Sci. Adv. **5**, eaaw5685 (2019).

[21] M. M. Otrokov *et al.*, arXiv:1809.07389.

[22] D. S. Lee, T.-H. Kim, C.-H. Park, C.-Y. Chung, Y. S. Lim, W.-S. Seo, and H.-H. Park, CrystEngComm **15**, 5532 (2013).

[23] J.-Q. Yan, Q. Zhang, T. Heitmann, Z. Huang, K. Y. Chen, J.-G. Cheng, W. Wu, D. Vaknin, B. C. Sales, and R. J. McQueeney, Phys. Rev. Materials **3**, 064202 (2019).

[24] R. C. Vidal *et al.*, arXiv:1903.11826.

[25] M. M. Otrokov, I. P. Rusinov, M. Blanco-Rey, M. Hoffmann, A. Yu. Vyazovskaya, S. V. Eremeev, A. Ernst, P. M. Echenique, A. Arnau, and E. V. Chulkov, Phys. Rev. Lett. **122**, 107202 (2019).

[26] Y. Peng and Y. Xu, Phys. Rev. B **99**, 195431 (2019).

[27] Y. Deng, Y. Yu, M. Zhu Shi, J. Wang, X. H. Chen, and Y. Zhang, arXiv:1904.11468.

[28] C. Liu *et al.*, arXiv:1905.00715.

[29] See Supplemental Material at http://link.aps.org/supplemental/10.1103/PhysRevResearch.1.012011 for details of crystal growth, scanning transmission electron microscope, ARPES, magnetization, neutron diffraction, high-magnetic field magnetotransport measurement and torque simulations.

[30] R. S. K. Mong, A. M. Essin, and J. E. Moore, Phys. Rev. B **81**, 245209 (2010).

[31] T. J. Liu *et al.*, Phys. Rev. B **80**, 174509 (2009).

[32] M. N. Baibich, J. M. Broto, A. Fert, F. N. Vandau, F. Petroff, P. Eitenne, G. Creuzet, A. Friederich, and J. Chazelas, Phys. Rev. Lett. **61**, 2472 (1988).

[33] G. Binasch, P. Grunberg, F. Saurenbach, and W. Zinn, Phys. Rev. B **39**, 4828 (1989).

[34] M. Zhu, T. Hong, J. Peng, T. Zou, Z. Q. Mao, and X. Ke, J. Phys.: Condens. Matter **30**, 075802 (2018).

[35] C. Z. Chang *et al.*, Phys. Rev. Lett. **112**, 056801 (2014).

[36] D.-X. Qu, Y. S. Hor, J. Xiong, R. J. Cava, and N. P. Ong, Science **329**, 821 (2010).

[37] K. Shrestha, M. Chou, D. Graf, H. D. Yang, B. Lorenz, and C. W. Chu, Phys. Rev. B **95**, 195113 (2017).

[38] J. P. Fleurial, L. Gailliard, R. Triboulet, H. Scherrer, and S. Scherrer, J. Phys. Chem. Solids **49**, 1237 (1988).

[39] T. Suzuki, R. Chisnell, A. Devarakonda, Y. T. Liu, W. Feng, D. Xiao, J. W. Lynn, and J. G. Checkelsky, Nat. Phys. **12**, 1119 (2016).

[40] N. Nagaosa, J. Sinova, S. Onoda, A. H. MacDonald, and N. P. Ong, Rev. Mod. Phys. **82**, 1539 (2010).

[41] S. Nakatsuji, N. Kiyohara, and T. Higo, Nature (London) **527**, 212 (2015).

[42] H. Chen, Q. Niu, and A. H. MacDonald, Phys. Rev. Lett. **112**, 017205 (2014).